σ_n indicates a coning motion in excess of 30 deg after 8 s of flight. At this time, the slope of the Euler spin $\dot{\phi}$ changes by a factor of 10. Thus, projectiles fully filled with liquid show the same spin-down behavior as projectiles with moving rigid payloads. Indeed, this large despin moment occurring for payload-induced instability was suggested by Miller[7] as a design tool, a technique justified by flight tests.[8]

The first theoretical relation between side moment and roll moment for liquid payloads in a cylindrical container was given in Ref. 9. This reference assumed that the steady-state motion of a liquid could be approximated by a linearized Navier-Stokes equation and then showed (after considerable algebra) that Eq. (3) was valid for a liquid payload. Later, Rosenblat et al.[10] showed that linearization of the Navier-Stokes equation was unnecessary. After three pages of much simpler algebra, Ref. 10 showed that any liquid in a fully filled cylindrical cavity (provided the liquid satisfies the continuity equation and is in steady-state motion) has the following relationship between its side moment and its roll moment:

$$M_{px} = -M_{py} \tan \alpha_c \tag{4}$$

Note that the linear versions of Eqs. (3) and (4) are the same but Eq. (4), which is based on the nonlinear Navier-Stokes equations, is the more accurate nonlinear version.

General Moving Payload Moment Relation

The occurrence of Eq. (4) in so many moving payload theories suggests the possibility that some simple general proof of this relation should exist for all possible moving payloads in steady-state motion. Indeed, such a proof was developed in Ref. 11 by differentiating the angular momentum of the moving payload.

The moment exerted by the moving payload is the negative of the derivative of the payload's angular momentum:

$$\boldsymbol{M}_p = -(\dot{L}_1 \hat{e}_{xc} + \dot{L}_2 \hat{e}_{yc} + \dot{L}_3 \hat{e}_{zc} + \boldsymbol{\Omega} \times \boldsymbol{L}) \tag{5}$$

where (L_1, L_2, L_3) are the coning system components of the payload angular momentum vector.

For steady-state coning motion, $\dot{L}_j = 0$ and, hence,

$$\boldsymbol{M}_p = \dot{\phi}_c \left[-L_3 \sin \alpha_c \hat{e}_{xc} + L_3 \cos \alpha_c \hat{e}_{yc} + (L_1 \sin \alpha_c - L_2 \cos \alpha_c) \hat{e}_{zc} \right] \tag{6}$$

so that

$$M_{px} = -M_{py} \tan \alpha_c \tag{7}$$

Conclusions

The presence of a payload-induced side moment can always be identified by the roll moment for large coning motion. Even more importantly, the payload side moment can be measured in ground tests by measurement of the spin moment exerted by a payload doing a forced coning motion.

References

[1]Murphy, C. H., "Free Flight Motion of Symmetric Missiles," U.S. Army Ballistic Research Laboratory, Aberdeen Proving Ground, MD, Rept. 1216, AD 442757, July 1963.

[2]Karpov, B. G., and Bradley, J. W., "A Study of Causes of Short Ranges of the 8 Inch, T317 Shell," U.S. Army Ballistic Research Laboratory, Aberdeen Proving Ground, MD, Rept. 1049, AD 377548, May 1958.

[3]Chadwick, W. R., "Stability of Spinning Shell (Influence of Elastically Supported Gyroscopic Mass)," unpublished Naval Surface Weapons Center manuscript, Dahlgren, VA, Sept. 1975.

[4]Soper, W. G., "Projective Instability Produced by Internal Friction," *AIAA Journal*, Vol. 16, No. 1, 1978, pp. 8-11.

[5]Murphy, C. H., "Influence of Moving Internal Parts on Angular Motion of Spinning Projectiles," *Journal of Guidance and Control*, Vol. 1, No. 2, 1978, pp. 117-122; see also BRL-MR-2731, AD A037338, Feb. 1977.

[6]D'Amico, W. P., Oskay, V., and Clay, W. H., "Flight Tests of the 155mm XM687 Binary Projectile and Associated Design Modifications Prior to the Nicolet Winter Test 1974-1975," U.S. Army Ballistic Research Laboratory, Aberdeen Proving Ground, MD, MR 2748, AD B019969, May 1977.

[7]Miller, M. C., "Flight Instabilities of Spinning Projectiles Having Nonrigid Payloads," *Journal of Guidance, Control, and Dynamics*, Vol. 5, No. 2, 1982, pp. 151-157.

[8]D'Amico, W. P., and Miller, M. C., "Flight Instability Produced by a Rapidly Spinning, Highly Viscous Liquid," *Journal of Spacecraft and Rockets*, Vol. 16, No. 1, 1976, pp. 62-64.

[9]Murphy, C. H., "Liquid Payload Roll Moment Induced by a Spinning and Coning Projectile," U.S. Army Ballistic Research Laboratory, Aberdeen Proving Ground, MD, ARBRL-TR-02521, AD A133681, Sept. 1983; also, AIAA Paper 83-2142, Aug. 1983.

[10]Rosenblat, S., Gooding, A., and Engleman, M. S., "Finite Element Calculations of Viscoelastic Fluid Flow in a Spinning and Nutating Cylinder," U.S. Army Armament Munitions Chemical Command, Aberdeen Proving Ground, MD, CRDEC-CR-87021, Dec. 1986.

[11]Murphy, C. H., Bradley, J. W., and Mermagen, W. H., Sr., "Side Moment Induced by a Spinning, Coning, Highly Viscous Liquid Payload," U.S. Army Ballistic Research Laboratory, Aberdeen Proving Ground, MD, BRL-TR-3074, AD 218746, Dec. 1989.

Two Variations of Certainty Control

Salvatore Alfano*
U.S. Air Force Academy,
Colorado Springs, Colorado 80840

Introduction

CERTAINTY control[1] enhances interceptor performance by using a terminal guidance law that incorporates the dynamics of the interceptor and target plus the error knowledge of their estimates. This is done by constraining the final estimated state to a spherical inequality based on the projected estimate error. The control law reduces intercept maneuvering when the controls associated with cost do not affect state estimate certainty.[2]

Two variations of certainty control are presented in an attempt to further improve interceptor performance: the first uses a control effectiveness ratio to regulate thrusting times; the second changes the certainty control constraint to an ellipsoidal function based on projected estimate error. Conceptually, the second variation produces a shrinking ellipsoid about the predicted impact point with the surface being a function of estimated error; if the predicted miss is inside or touching the ellipsoid, thrusting is not necessary.

Variational performances in lateral thrusting are examined for a hypervelocity, exoatmospheric, orbital vehicle in the final 30 s of flight while it is attempting to intercept a boosting missile. System modeling and measurement processing are identical to those used in Ref. 1. Target tracking is accomplished with a ranging device and line-of-sight sensors for in-plane and out-of-plane measurements. Noise-corrupted data are processed through an eight-state extended Kalman filter (EKF) with serial updates occurring every 0.1 s. Velocity changes are determined by varying impact conditions using splines to reduce computational burdens and allow a solution that lends itself to deterministic techniques.

Optimum Spacing of Corrective Thrusts

Corrective thrusting in the presence of state estimate errors can be optimally spaced to reduce fuel. A control effectiveness

Received Aug. 5, 1991; revision received Oct. 29, 1991; accepted for publication Nov. 16, 1991.

*Associate Professor, Deputy for Labs and Research, Department of Astronautics. Senior Member AIAA.

ratio,[3] ρ, is established to determine the spacing between thrusts; the ratio directly yields thrust times when control effectiveness is a linear function of time. Control effectiveness is measured by the amount the end conditions vary for a specified control; for this problem, as intercept time decreases, so does the ability of lateral thrusting to vary miss distance. With a ratio of two ($\rho = 2.0$), the corrective thrusting should only occur when the control has half the effect ($1/\rho$) of the previous corrective thrust. If control effectiveness is a near-linear function of time, as is the case for a hypervelocity orbital vehicle, then it will be halved at about half the time to impact since the last thrust. Thrusting will occur at the start of the intercept, at one-half time-to-go, one-fourth time-to-go, one-eighth time-to-go, etc. When spacing is less than the estimator's cycle time (0.1 s for this study), impact is imminent and thrust is terminated.

Certainty Control Formulation with Ellipsoidal Constraint

As stated earlier, if the controls associated with cost do not affect state estimate certainty, then fuel may be conserved by using that certainty to reduce control efforts. When the controls are linked to the estimate certainty, a near-perfect estimate yields the optimal control (certainty equivalence solution[4]), and a poor estimate causes a reduction in control. Certainty control does this by constraining the final estimated states to a spherical inequality based on the projected estimate error. An ellipsoidal inequality is introduced by establishing the cost function,

$$L = \frac{\Delta V_y^2 + \Delta V_z^2}{2} \tag{1}$$

subject to the following constraint:

$$f = \frac{\hat{x}_f^2}{2\sigma_{xf}^2} + \frac{\hat{y}_f^2}{2\sigma_{yf}^2} + \frac{\hat{z}_f^2}{2\sigma_{zf}^2} - \frac{K}{2} \le 0 \tag{2}$$

where ΔV_y and ΔV_z are the interceptor's velocity changes, and K is the constraint weighting factor. Time-to-go t_{go} is used as a third control parameter to minimize miss distance but does not explicitly appear in the cost function. The final state estimates $(\hat{x}_f, \hat{y}_f, \hat{z}_f)$ and their deviations $(\sigma_{xf}, \sigma_{yf}, \sigma_{zf})$ are determined by running the filter forward to predicted impact time without measurement or control updates and then representing their time history with splines:

$$x_s = A_x t_{go}^3 + B_x t_{go}^2 + C_x t_{go} + D_x \tag{3}$$

$$y_s = A_y t_{go}^3 + B_y t_{go}^2 + C_y t_{go} + D_y \tag{4}$$

$$z_s = A_z t_{go}^3 + B_z t_{go}^2 + C_z t_{go} + D_z \tag{5}$$

$$\hat{x}_f = x_s \tag{6}$$

$$\hat{y}_f = y_s - \Delta V_y t_{go} \tag{7}$$

$$\hat{z}_f = z_s - \Delta V_z t_{go} \tag{8}$$

$$\sigma_{xf} = A_{\sigma x} t_{go}^3 + B_{\sigma x} t_{go}^2 + C_{\sigma x} t_{go} + D_{\sigma x} \tag{9}$$

$$\sigma_{yf} = A_{\sigma y} t_{go}^3 + B_{\sigma y} t_{go}^2 + C_{\sigma y} t_{go} + D_{\sigma y} \tag{10}$$

$$\sigma_{zf} = A_{\sigma z} t_{go}^3 + B_{\sigma z} t_{go}^2 + C_{\sigma z} t_{go} + D_{\sigma z} \tag{11}$$

Conceptually, the constraint produces a deviation ellipsoid about the predicted impact point. If the predicted miss is inside or touching the ellipsoid, then thrusting is not necessary. If the predicted miss is outside the ellipsoid, then minimum thrusting is determined to bring the miss to the ellipsoid's surface. Sensor inaccuracies will cause the predicted impact point (ellipsoid center) to jitter with each measurement; chasing this point (i.e., attempting a zero-miss solution) results in counterproductive maneuvering. As the estimates improve, the constraint tightens and the ellipsoid shrinks, along with predicted miss distance. The spline representations allow this stochastic problem to be solved in a deterministic fashion[5] by adjoining the constraint to the cost function to form the Hamiltonian:

$$H = L + \lambda f \tag{12}$$

where λ is the Lagrangian multiplier. The partials of H with respect to the controls must equal zero:

$$\frac{\partial H}{\partial \Delta V_y} = \Delta V_y - \frac{\lambda \hat{y}_f t_{go}}{\sigma_{yf}^2} = 0 \tag{13}$$

$$\frac{\partial H}{\partial \Delta V_z} = \Delta V_z - \frac{\lambda \hat{z}_f t_{go}}{\sigma_{zf}^2} = 0 \tag{14}$$

$$\frac{\partial H}{\partial t_{go}} = \lambda\left(\frac{\hat{x}_f \dot{\hat{x}}_f}{\sigma_{xf}^2} + \frac{\hat{y}_f \dot{\hat{y}}_f}{\sigma_{yf}^2} + \frac{\hat{z}_f \dot{\hat{z}}_f}{\sigma_{zf}^2} - \frac{\hat{x}_f^2 \dot{\sigma}_{xf}}{\sigma_{xf}^3} - \frac{\hat{y}_f^2 \dot{\sigma}_{yf}}{\sigma_{yf}^3} - \frac{\hat{z}_f^2 \dot{\sigma}_{zf}}{\sigma_{zf}^3}\right) = 0 \tag{15}$$

with

$$\dot{\hat{x}}_f = 3A_x t_{go}^2 + 2B_x t_{go} + C_x \tag{16}$$

$$\dot{\hat{y}}_f = 3A_y t_{go}^2 + 2B_y t_{go} + C_y - \Delta V_y \tag{17}$$

$$\dot{\hat{z}}_f = 3A_z t_{go}^2 + 2B_z t_{go} + C_z - \Delta V_z \tag{18}$$

$$\dot{\sigma}_{xf} = 3A_{\sigma x} t_{go}^2 + 2B_{\sigma x} t_{go} + C_{\sigma x} \tag{19}$$

$$\dot{\sigma}_{yf} = 3A_{\sigma y} t_{go}^2 + 2B_{\sigma y} t_{go} + C_{\sigma y} \tag{20}$$

$$\dot{\sigma}_{zf} = 3A_{\sigma z} t_{go}^2 + 2B_{\sigma z} t_{go} + C_{\sigma z} \tag{21}$$

Equations (2), (13), (14), and (15) constitute four equations with four unknowns, which can be reduced to two equations and two unknowns using Eqs. (7) and (8). Substituting Eq. (7) into Eq. (13) yields

$$\Delta V_y = \frac{\lambda y_s t_{go}}{\sigma_{yf}^2 + \lambda t_{go}^2} \tag{22}$$

$$\hat{y}_f = \frac{y_s \sigma_{yf}^2}{\sigma_{yf}^2 + \lambda t_{go}^2} \tag{23}$$

In a similar manner, substituting Eq. (8) into Eq. (14) yields

$$\Delta V_z = \frac{\lambda z_s t_{go}}{\sigma_{zf}^2 + \lambda t_{go}^2} \tag{24}$$

$$\hat{z}_f = \frac{z_s \sigma_{zf}^2}{\sigma_{zf}^2 + \lambda t_{go}^2} \tag{25}$$

Equations (2) and (15) can now be solved in terms of λ and t_{go}, with ΔV_y and ΔV_z determined afterward from Eqs. (22) and (24). The parameters λ and t_{go} can be found by numerical techniques using the Jacobian:

$$[J]\begin{bmatrix} dt_{go} \\ d\lambda \end{bmatrix} = \begin{bmatrix} -f_1 \\ -f_2 \end{bmatrix} \tag{26}$$

$$f_1 = \frac{\hat{x}_f^2}{2\sigma_{xf}^2} + \frac{\hat{y}_f^2}{2\sigma_{yf}^2} + \frac{\hat{z}_f^2}{2\sigma_{zf}^2} - \frac{K}{2} \tag{27}$$

$$f_2 = \lambda\left(\frac{\hat{x}_f \dot{\hat{x}}_f}{\sigma_{xf}^2} + \frac{\hat{y}_f \dot{\hat{y}}_f}{\sigma_{yf}^2} + \frac{\hat{z}_f \dot{\hat{z}}_f}{\sigma_{zf}^2} - \frac{\hat{x}_f^2 \dot{\sigma}_{xf}}{\sigma_{xf}^3} - \frac{\hat{y}_f^2 \dot{\sigma}_{yf}}{\sigma_{yf}^3} - \frac{\hat{z}_f^2 \dot{\sigma}_{zf}}{\sigma_{zf}^3}\right) \tag{28}$$

$$J = \begin{bmatrix} \dfrac{\partial f_1}{\partial t_{go}} & \dfrac{\partial f_1}{\partial \lambda} \\ \dfrac{\partial f_2}{\partial t_{go}} & \dfrac{\partial f_2}{\partial \lambda} \end{bmatrix} \tag{29}$$

If the states are perfectly known, the σ terms will be zero and the constraint of Eq. (2) will only be satisfied with a predicted miss of zero; the ellipsoidal certainty control equations reduce to the certainty equivalence optimal-control formulation.[1] If the estimate is poor, the σ terms will be large and the inequality constraint of Eq. (2) will result in very little, if any, change in velocity.

Computer Simulation

A head-on, 10-deg out-of-plane intercept is examined with a time-to-go of 30 s. The interceptor is initially traveling at 12 km/s at an altitude of 750 km with a lateral acceleration range of 3–60 m/s^2 in each axis. The booster's initial acceleration is 3.15788 m/s^2, with a unitized mass flow rate of 0.01579 s^{-1}.

A time lag of 0.1 s is used when computing velocity changes to account for measurement processing, controller processing, and thruster response. Target acquisition is assumed to take 3 s; thrusting is not permitted during this time. This simulation, written in Fortran 77 to run on a VAX 3600, generates 200 Monte Carlo runs per case.

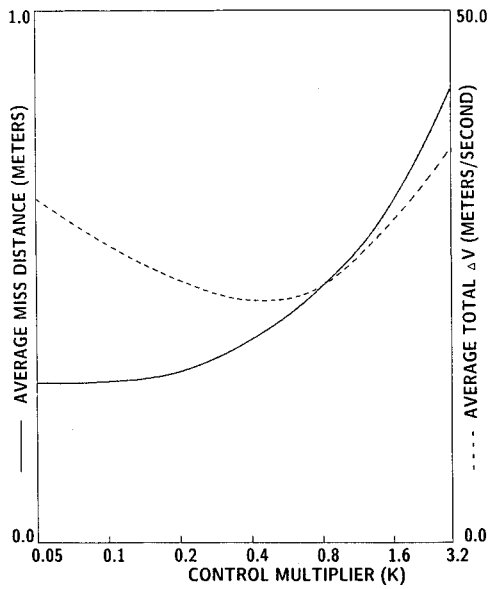

Fig. 1 Performance of certainty control for head-on, 10-deg out-of-plane intercept.

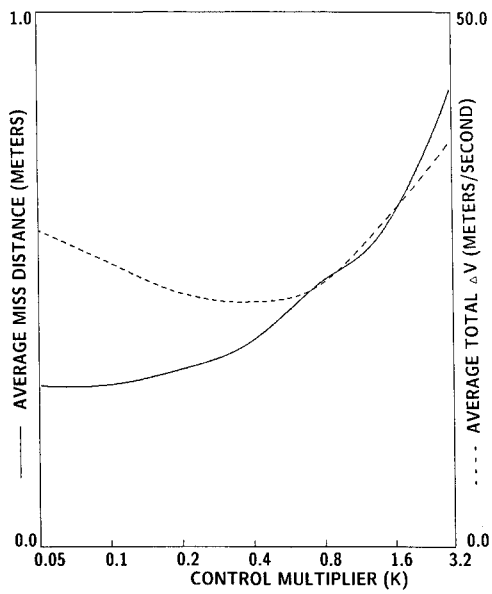

Fig. 2 Performance of certainty control for head-on, 10-deg out-of-plane intercept with $\rho = 1.1$.

Table 1 Minimum ΔV performance for 10-deg out-of-plane intercept

(ellipsoidal constraint) Control strategy	multiplier, K Control multiplier, K	ΔV, m/s ΔV, m/s	distance, m Miss distance, m
Certainty control (original formulation)	0.472	23.13	0.404
Certainty control ($\rho = 1.1$)	0.383	23.26	0.383
Certainty control (ellipsoidal constraint)	1.457	21.88	0.476

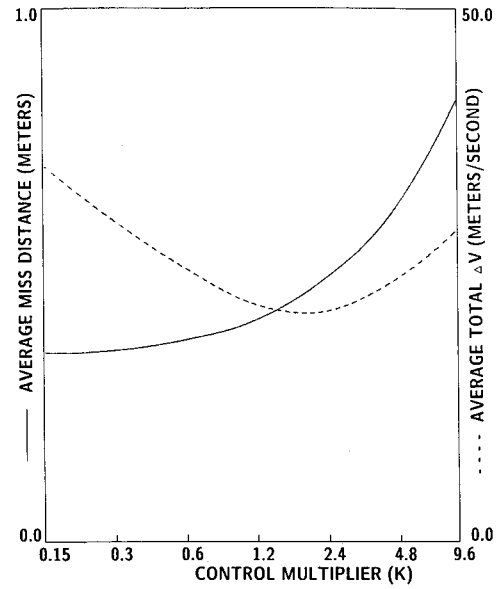

Fig. 3 Performance of ellipsoidal constraint control for head-on, 10-deg out-of-plane intercept.

Results

The original certainty control performance serves as a basis of comparison for the variations, with Fig. 1 showing the relationships of miss distance and total ΔV to the constraint parameter K. Figure 2 illustrates the relationships when the thrusting times are limited by a control effectiveness ratio of 1.1, and Fig. 3 shows the effect of altering the control constraint from spherical to ellipsoidal.

The minimum ΔV performances of all three control strategies are found in Table 1. A control effectiveness ratio of 1.1 slightly reduces the miss distance and increases the total ΔV, whereas larger ratios degrade performance for this particular intercept. Reformulating the control law using an ellipsoidal constraint reduces the total ΔV, but sacrifices some accuracy. Although they are inconclusive, these results indicate that the original formulation of certainty control effectively uses the state deviations to minimize maneuvering costs while maintaining a high level of accuracy.

Conclusions

In this Note, two variations of certainty control were examined to determine their capability to minimize lateral velocity changes of a hypervelocity orbital vehicle in a head-on, 10-deg out-of-plane intercept. The first variation used a control effectiveness ratio to regulate thrusting times; the second changed the spherical constraint function to an ellipsoidal one. Neither variation simultaneously reduced maneuvering cost and miss distance when compared to the original formulation of certainty control, indicating that the original formulation of certainty control effectively uses the state deviations to minimize maneuvering costs while maintaining a high level of accuracy. The ellipsoidal variation best demonstrated a tradeoff in accuracy to reduce maneuvering costs, a choice to be made

based on mission constraints. An area of further research is to find a way to make better use of the state deviations in formulating the control law, i.e., reducing cost while further improving accuracy.

References

[1]Alfano, S., and Fosha, C. E., Jr., "Hypervelocity Orbital Intercept Guidance Using Certainty Control," *Journal of Guidance, Control, and Dynamics,* Vol. 14, No. 3, 1991, pp. 574-580.

[2]Alfano, S., "Hypervelocity Orbital Intercept Guidance," Ph.D. Dissertation, Electrical Engineering Dept., Univ. of Colorado, Colorado Springs, CO, 1988.

[3]Leitmann, G., *Optimization Techniques,* Academic, New York, 1962, pp. 353-357.

[4]Aoki, M., *Optimization of Stochastic Systems,* Academic, New York, 1967, p. 10.

[5]Bryson, A. E., and Ho, Y. C., *Applied Optimal Control,* Hemisphere, Washington, DC, 1975, pp. 71-75.

Man-in-the-Loop Study of Filtering in Airborne Head Tracking Tasks

S. Lifshitz* and S. J. Merhav†
Technion—Israel Institute of Technology, Haifa, Israel

Nomenclature

a, a' = acceleration
g = gravity acceleration
N_{na} = nonadditive, nonvoluntary head motion
$\hat{N}_{na}$ = estimated nonadditive, nonvoluntary head motion
U_b = nonvoluntary head motion
$\hat{U}_b$ = estimated additive nonvoluntary head motion
U_c = voluntary head motion
U_f = estimated voluntary head motion
U_t = total head motion
Y_b = biodynamic transfer function
α, α_r = angles

Introduction

ONBOARD head tracking of targets by means of helmet mounted sights (HMS) for teleoperation of cameras, lasers, or antennas is often subjected to dynamical interferences that affect the precision required in such tasks. These interferences, which result from aircraft motion and vibration, consist of an additive component correlated with the aircraft vibration and a nonadditive component known as remnant. These interferences, called biodynamic interferences,[1,2] cause vision blurring in helmet mounted displays (HMD)[3,4] and degradation of tracking and pointing accuracy.[5,6] A method to reduce these effects by estimating in real time the nonvoluntary components of head motion and to use these signals to stabilize the symbols in the image plane of the display, thus reducing blurring in viewing tasks, has been described by Lifshitz and Merhav.[7] In this Note, we address the problems caused by the vibrations while using an HMS in tracking tasks, where the major effects are the head vibration and target motion.[5] Tatham[8] investigated, with some success, methods for improving tracking precision by means of various filtering schemes of the signal sent to the teleoperated device. Tatham used low-pass filtering of the total teleoperation command, thus perhaps improving smoothness of the motion of the teleoperated device, but sacrificing pointing agility.

The method presented in this Note for improving aiming accuracy in tracking tasks is based on head motion measurement and on the shifting of the reticle in the HMD in such a way as to inhibit much of the nonvoluntary apparent motion of the reticle relative to the target and the nonvoluntary motion of the teleoperated device. The HMD also inherently provides the required visual feedback.

Principle of Operation

The method for stabilization of a true HMS is described in detail in Ref. 7. The head motion sensor provides head position and orientation signals with respect to the cockpit. These signals consist of the voluntary head motion U_c and the nonvoluntary head motion U_b. The total head motion is defined as $U_t = U_c + U_b$. The adaptive algorithm provides estimated values $\hat{U}_b$ of U_b and U_f of U_c, which are derived from $U_f = U_t - \hat{U}_b$. To facilitate smooth head teleoperation, additional filtering must be provided to compensate for the nonadditive, nonvoluntary head motion components N_{na}. Not being correlated with the cockpit motion, they cannot be suppressed by the adaptive algorithm. They give rise to additional relative shifts between the eye and the display and impair target acquisition and tracking. U_c is by nature of a much lower frequency than U_b. Therefore, U_f, which is an estimate of U_c, is low-pass filtered to provide the signal fed to the teleoperated device. To stabilize the HMS, U_f is high-pass filtered to provide the estimated nonadditive, nonvoluntary head motion $\hat{N}_{na}$, which is added to $\hat{U}_b$, and both are fed into the display generator in opposite phase with the head motion. The result is a less blurred sight, stabilized against the effects of U_b and N_{na}.

Experimental Investigation and Set-Up

The experimental program had two main goals: 1) to determine the effects of vibration on head pointing accuracy, and 2) to quantify the contribution of the various filtering schemes to head pointing precision.

The laboratory simulation facility used in the experiments consisted of a six-degree-of-freedom motion base simulator with a bandwidth of 15 Hz and a maximum acceleration capability of $1g$. Lack of an actual HMS/HMD and time lags caused by the head motion sensor, a magnetic Polhemus 3 space head tracker, required that an emulation of a sight be used in place of an actual HMS, as illustrated in Fig. 1. The sight emulation incorporated an overhead TV projector to

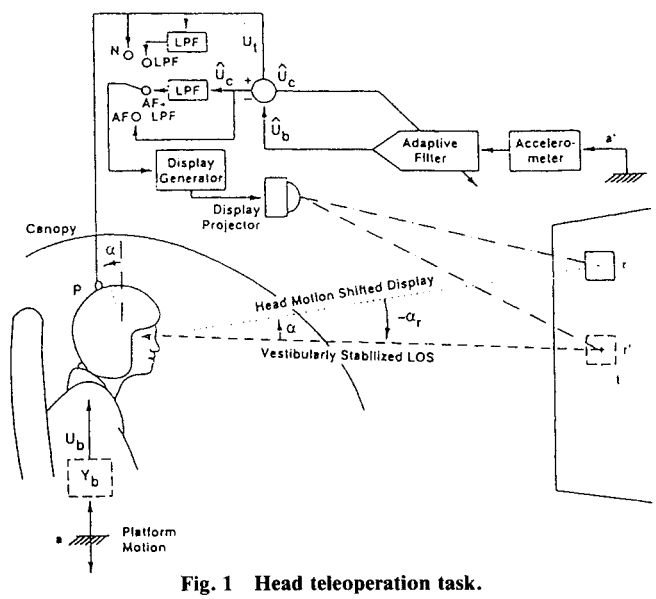

Fig. 1 Head teleoperation task.

Received Oct. 5, 1990; revision received July 8, 1991; accepted for publication Aug. 25, 1991.

*Graduate Student, Department of Aerospace Engineering.
†Professor, Head, Flight Control Laboratory, Department of Aerospace Engineering.